Provided for non-commercial research and education use.
Not for reproduction, distribution or commercial use.

This article appeared in a journal published by Elsevier. The attached copy is furnished to the author for internal non-commercial research and education use, including for instruction at the authors institution and sharing with colleagues.

Other uses, including reproduction and distribution, or selling or licensing copies, or posting to personal, institutional or third party websites are prohibited.

In most cases authors are permitted to post their version of the article (e.g. in Word or Tex form) to their personal website or institutional repository. Authors requiring further information regarding Elsevier's archiving and manuscript policies are encouraged to visit:

http://www.elsevier.com/copyright

Author's personal copy

Computers & Fluids 39 (2010) 1585–1596

Contents lists available at ScienceDirect

Computers & Fluids

journal homepage: www.elsevier.com/locate/compfluid

Multi-level adaptive simulation of transient two-phase flow in heterogeneous porous media

C.C. Chueh [a], M. Secanell [a], W. Bangerth [b], N. Djilali [a,*]

[a] Institute for Integrated Energy Systems and Department of Mechanical Engineering, University of Victoria, PO Box 3055 STN CSC, Victoria, BC, Canada V8W 3P6
[b] Department of Mathematics, Texas A&M University, College Station, TX 77843-3368, USA

ARTICLE INFO

Article history:
Received 17 November 2009
Received in revised form 6 May 2010
Accepted 17 May 2010
Available online 2 June 2010

Keywords:
Two-phase flow
Heterogeneous porous media
Adaptive mesh refinement
Stabilized finite element method

ABSTRACT

An implicit pressure and explicit saturation (IMPES) finite element method (FEM) incorporating a multi-level shock-type adaptive refinement technique is presented and applied to investigate transient two-phase flow in porous media. Local adaptive mesh refinement is implemented seamlessly with state-of-the-art artificial diffusion stabilization allowing simulations that achieve both high resolution and high accuracy. Two benchmark problems, modelling a single crack and a random porous medium, are used to demonstrate the robustness of the method and illustrate the capabilities of the adaptive refinement technique in resolving the saturation field and the complex interaction (transport phenomena) between two fluids in heterogeneous media.

© 2010 Elsevier Ltd. All rights reserved.

1. Introduction

Modelling of two-phase flow in porous media plays a key role in many engineering areas such as environmental remediation [1,2], oil recovery [3–6] and water management in polymer electrolyte fuel cells [7–12]. In polymer electrolyte fuel cells, which motivated in part the developments described herein, water produced at the cathode as a result of the electrochemical reaction can condense [7,8], and is eventually transported through the porous electrode by a combination of mechanisms, including capillary diffusion. At high reaction rates however, an imbalance between liquid water production and transport can result in flooding of the electrode and, consequently, restricted access of the reactant gases to the reactions sites (catalyst layer); this results in a significant performance drop. Understanding of the two-phase transport processes and design of the porous media to mitigate this are therefore crucial and can be facilitated by robust and physically representative simulations. A number of recent publications have addressed some of the modelling challenges associated with two-phase transport in complex porous media. These include the development of improved numerical schemes for simulation of multi-phase, multi-component processes [13]; interface conditions and linearization schemes [14]; advanced numerical procedures based on high-order time integration schemes [15], fractional flow approaches [16], and reduced degrees of freedom [17]. Theoretical investigations based on pore-network models [18], non-oscillation central scheme [19], and multi-scale finite volume/element methods [20–24] have also been developed. Helmig et al. [25] note that numerical methods have to be able to capture both advection or diffusion/dispersion dominated processes. An excellent review of the recent modelling efforts and current challenges is provided by Gerritsen and Durlofsky [5]. A key challenge remains the robust and accurate resolution of fine-scale localized flow.

In transient two-phase flow simulations related to petroleum engineering, the implicit pressure and explicit saturation (IMPES) algorithm, originally developed by Sheldon et al. [26] and Stone and Gardner [27], is widely used. The basic idea of this classical method when applied to two-phase flow in porous media is to separate the computation of pressure from that of saturation. Namely, the coupled system is split into a pressure equation and a saturation equation, and the pressure and saturation equations are solved using implicit and explicit time approximation approaches, respectively. This method is easy to implement and efficient to solve, and requires less memory than other methods such as the simultaneous solution method [28]. Detailed discussions of this method can be found in [26,27], and recent algorithmic improvements are discussed in Chen et al. [29,30].

The numerical simulation of transient two-phase flow transport in heterogeneous porous media (Fig. 1) is computationally expensive, and adequate resolution of complex flow features is not always possible, thus compromising the reliability of the results. Achieving physically representative simulations that resolve all salient length and time scales and localized flow features efficiently remains a challenge. An alternative to global mesh refinement which demands very large computing resources, is adaptive mesh

* Corresponding author. Tel.: +1 250 721 6034; fax: +1 250 721 6323.
E-mail address: ndjilali@uvic.ca (N. Djilali).

0045-7930/$ - see front matter © 2010 Elsevier Ltd. All rights reserved.
doi:10.1016/j.compfluid.2010.05.011

Author's personal copy

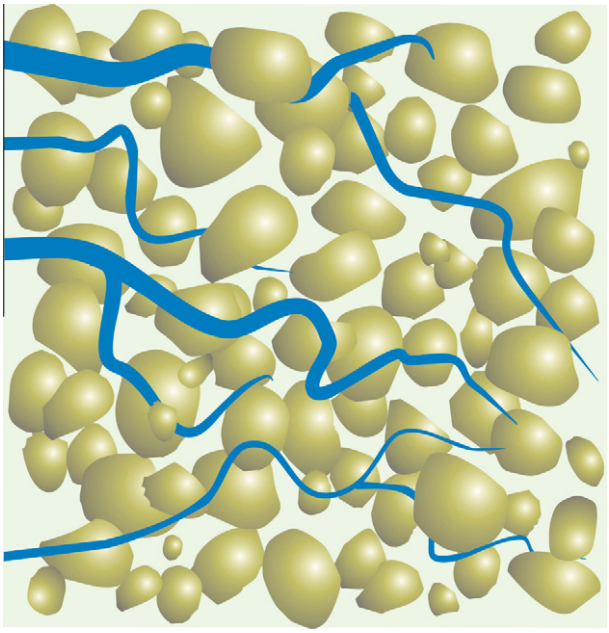

Fig. 1. Schematic of fluid flow in a heterogeneous porous medium.

refinement (AMR). A variety of AMR methods have been proposed depending on the type of physical problem and associated partial differential equations (PDE), and a large body of literature [31–33] exists for these methods. One can use a simple refinement indicator, such as those proposed in [34], to refine and coarsen the mesh at each time step, depending on where the discontinuities (phase boundaries in the present context) propagate. Recent work by Noelle et al. [35] shows that a central scheme with AMR can be implemented on non-conforming 3D Cartesian grids to extend the classical hydrodynamics AMR framework [30]. Smoothness indicators for conservation laws were developed by [36]. Another approach to adaption is the use of a moving-mesh method such as that of Tang and Tang [37] to align the mesh with the important features of the flow. In any case, the major advantages of using grid adaption are high-quality resolution of the physical features as they evolve in space and time while simultaneously reducing computational cost by refining only in areas where necessary and coarsening in areas where unnecessarily fine grids exist. Note that in the context of multi-phase flow the porous medium is frequently strongly heterogeneous within the computational domain. However, as we will show below, there is no need to resolve these heterogeneities everywhere unless they interact with flow fronts. Consequently, adaptive mesh refinement has the potential to significantly reduce the computational cost of multi-phase flow simulations. Despite these obvious advantages, the literature is relatively limited for transient adaptive methods suitable for multi-phase flow in porous media.

When a general continuous finite element discretization is adopted for the saturation transport (advection) equation in two-phase flow problems, spurious and unphysical oscillations appear in the solution, requiring the introduction of a stabilizing (diffusive) term [38]. However, this results in smearing of sharp fronts and can also cause grid-orientation difficulties [38]. Finding the right balance between preserving accuracy and providing stability is therefore of great importance in the numerical solution of conservation laws. In this work, we implement the artificial diffusion terms proposed by Guermond and Pasquetti [39]. This entropy-based nonlinear viscosity provides a powerful approach yielding both accuracy and stability. First, the artificial viscosity term acts only in the vicinity of strong gradients in the saturation and other discontinuities [39]; secondly, the term does not affect the solution in smooth regions; and finally the scheme offers higher order accuracy and stability than simple upwind schemes [39]. In this paper, this approach is combined with an IMPES algorithm and we present an extension of shock-type adaptive refinement to saturation gradients to investigate transient transport phenomena in heterogeneous porous media. The use of this shock-type adaptive refinement technique allows us to provide fine-scale resolution locally and to concentrate numerical efforts near the area where the two-phase interfaces evolve.

2. Basic numerical model

Let us consider the flow of two incompressible, immiscible fluids in a porous media domain $\Omega \subset \mathscr{R}^2$ in which the movement (displacement) of two fluids is dominated by viscous effects and the effects of gravity and capillary pressure are negligible. The two phases are referred to as wetting and non-wetting, and identified by subscripts w and nw, respectively. Thus in a water–oil system (hydrophilic case), water is the wetting and oil the non-wetting phase; in the and air–water system (hydrophobic case), air is the wetting phase and water the non-wetting phase. The mass-averaged velocity with which each of the two phases moves is determined by Darcy's law. It states that the velocity is proportional to the pressure gradient [5]:

$$\mathbf{u}_j = -\frac{k_{rj}(S)}{\mu_j}\mathbf{K}\cdot\nabla p, \tag{1}$$

where $\mathbf{u}_j$ is the velocity of phase $j = w, nw$, $\mathbf{K}$ is the permeability tensor, k_{rj} is the relative permeability of phase j, p is the pressure, and $\boldsymbol{\mu}_j$ is the viscosity of phase j. Finally, S is the saturation of the porous media defined as

$$S = \frac{V_w}{V_w + V_{nw}}, \tag{2}$$

where V_w and V_{nw} are the volume fraction of the wetting and non-wetting phases. In this work, the permeability tensor, $\mathbf{K}$, is a second-order diagonal tensor.

After combining Darcy's law with the mass conservation equation, the following set of equations is obtained [5]:

$$\mathbf{u}_t = -\mathbf{K}\lambda_t(S)\nabla p, \tag{3}$$

$$\nabla\cdot\mathbf{u}_t = q, \tag{4}$$

$$\epsilon\frac{\partial S}{\partial t} + \nabla\cdot(\mathbf{u}_t F(S)) = 0, \tag{5}$$

where λ_t is the total mobility, ϵ is the porosity, F is the fractional flow of the wetting phase, q is a source term, and $\mathbf{u}_t$ is the total velocity. These are given by:

$$\lambda_t(S) = \lambda_w + \lambda_{nw} = \frac{k_{rw}(S)}{\mu_w} + \frac{k_{rnw}(S)}{\mu_{nw}}, \tag{6}$$

$$F(S) = \frac{\lambda_w}{\lambda_t} = \frac{\lambda_w}{\lambda_w + \lambda_{nw}} = \frac{k_{rw}(S)/\mu_w}{k_{rw}(S)/\mu_w + k_{rnw}(S)/\mu_{nw}}, \tag{7}$$

$$\mathbf{u}_t = \mathbf{u}_w + \mathbf{u}_{nw} = -\lambda_t(S)\mathbf{K}\cdot\nabla p. \tag{8}$$

For the sake of simplicity, we consider the case with no source term q. Furthermore the porosity ϵ is set to one as it is essentially a scaling factor that does not affect the qualitative behaviour of Eq. (5). For the purpose of this paper, we will assume the following concrete form for the total mobility λ_t and the fractional flow $F(S)$:

$$\lambda_t(S) = \frac{S^2}{\mu_w} + \frac{(1-S)^2}{\mu_{nw}}, \tag{9}$$

$$F(S) = \frac{S^2}{S^2 + 0.2\cdot(1-S)^2}, \tag{10}$$

where $\mu_w = 0.2$ and $\mu_{nw} = 1$.

Author's personal copy

2.1. Permeability of the porous media

In this and the following section, we will discuss the setup of the numerical examples used in Section 5. We consider a heterogeneous, isotropic porous medium with a permeability tensor $\mathbf{K}$ defined as

$$\mathbf{K}(\mathbf{x}) = k(\mathbf{x}) \cdot \mathbf{I} \tag{11}$$

where $k(\mathbf{x})$ is a scalar depending on position $\mathbf{x}$, and $\mathbf{I}$ is the second-order unit tensor. In order to demonstrate the robustness of the proposed shock-type adaptive refinement technique we consider the two model porous media used previously by Li and Bangerth [40]. The first test case corresponds to a single crack along a sine curve, with a permeability given by

$$k_{sm}(\mathbf{x}) = \max\left\{\exp\left(-\left(\frac{y - 0.5 - 0.1\cdot\sin(10x)}{0.1}\right)^2\right), 0.01\right\} \tag{12}$$

and $k(\mathbf{x})$ in Eq. (11) is replaced by $k_{sm}(\mathbf{x})$ for the first test case. Taking the maximum in Eq. (12) ensures boundedness of $k(x)$ from below.

The second test case corresponds to a porous medium with random permeability prescribed using

$$k_{rm}(\mathbf{x}) = \min\left\{\max\left\{\sum_{l=1}^{N}\Psi_l(\mathbf{x}), 0.01\right\}, 4\right\} \tag{13}$$

and

$$\Psi_l(\mathbf{x}) = \exp\left(-\left(\frac{|\mathbf{x} - \mathbf{x}_l|}{0.05}\right)^2\right) \tag{14}$$

where again $k_{rm}(\mathbf{x})$ is substituted for $k(\mathbf{x})$ in Eq. (11) for the second test case, and the centers $\mathbf{x}_l$ are N randomly chosen locations inside the domain. This function models a domain in which there are $N = 40$ centers of higher permeability, representing regions with cracks embedded in a matrix of intact background rock.

The permeability fields for these two testcases are shown in Fig. 2.

2.2. Initial and boundary conditions

The simulations are performed in a computational domain $\Omega = [0,1] \times [0,1]$ for $t \in [0,T]$. The initial condition is $S(\mathbf{x},0) = 0$, i.e. the reservoir contains only non-wetting fluid. Initial conditions for pressure or velocity are not necessary because the equations do not contain time derivatives of these variables. Finally, the following pressure boundary condition is used:

$$p(\mathbf{x},t) = 1 - x \quad \text{on } \partial\Omega \tag{15}$$

i.e. a linear pressure drop is assumed on the boundaries. Boundary conditions for the saturation need only be specified on the inflow part of the boundary given by

$$\Gamma_{in}(t) = \{\mathbf{x} \in \partial\Omega : \mathbf{n}\cdot\mathbf{u}_t < 0\}. \tag{16}$$

On the inflow boundary, we assume that wetting fluid enters the domain from the left, and consequently prescribe the following saturation values:

$$S(\mathbf{x},t) = 1 \quad \text{on } \Gamma_{in}(t) \cap \{x = 0\}, \tag{17}$$

$$S(\mathbf{x},t) = 0 \quad \text{on } \Gamma_{in}(t) \setminus \{x = 0\}. \tag{18}$$

3. Finite element approximations and numerical methods

The system of partial differential equations (PDE) Eqs. (3)–(5) that describes two-phase transport in a hydrophilic medium is discretized using a mixed finite element method [41,38]. The numerical solutions shown below were obtained using a C++ program based on the deal.II library [42]. The implementation discussed here also uses parts of the step-21, step-31 and step-33 tutorial programs of this library [40,43,44] but extends the functionality compared with all of these programs.

3.1. Time discretization

A standard implicit pressure and explicit saturation (IMPES) algorithm [26,27] is used for time discretization in conjunction with an implicit Euler method. In this algorithm, the pressure and velocity equations are first solved implicitly, and then the saturation equation is solved using an explicit time stepping method.

Using this time discretization, we obtain the following set of equations for each time step:

$$\mathbf{u}_t^{(n+1)} + \lambda_t(S^{(n)})\mathbf{K}\nabla p^{(n+1)} = 0, \tag{19}$$

$$\nabla\cdot\mathbf{u}_t^{(n+1)} = q, \tag{20}$$

$$\epsilon\left(\frac{S^{(n+1)} - S^{(n)}}{\Delta t^{(n+1)}}\right) + \mathbf{u}_t^{(n+1)}\cdot\nabla F(S^{(n)}) + F(S^{(n)})\nabla\cdot\mathbf{u}_t^{(n+1)} = 0, \tag{21}$$

where superscripts (n) and $(n+1)$ represent physical quantities existing at times $t^{(n)}$ and $t^{(n+1)}$, respectively, and $\Delta t^{(n)} = t^{(n+1)} - t^{(n)}$ is the length of the nth time step.

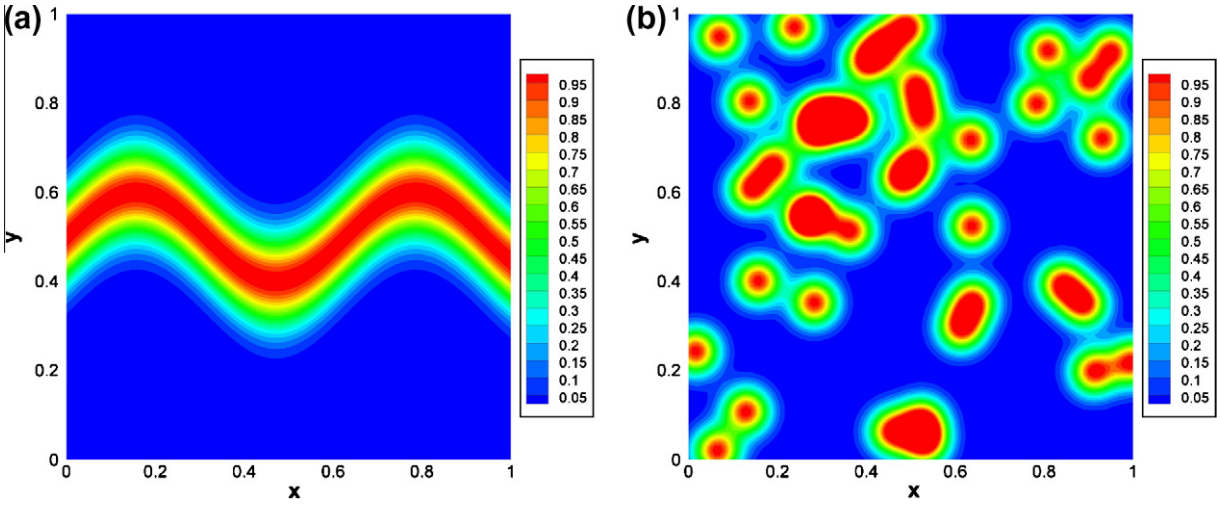

Fig. 2. Permeability fields for (a) single crack medium (b) random medium.

Author's personal copy

Using the fact that $\nabla \cdot \mathbf{u}_t = q$, Eq. (21) becomes

$$\epsilon\left(\frac{S^{(n+1)} - S^{(n)}}{\Delta t^{(n+1)}}\right) + \mathbf{u}_t^{(n+1)} \cdot \nabla F\left(S^{(n)}\right) + F(S^{(n)})q = 0. \tag{22}$$

To ensure stability of this time stepping scheme, the time step has to be chosen in accordance with the spatial discretization and satisfy the Courant–Friedrichs–Lewy (CFL) condition. In our numerical experiments, we choose the time step adaptively as

$$\Delta t^{(n+1)} = \frac{\min_K h_K}{7\|\mathbf{u}_t^{(n+1)}\|_{L^\infty(\Omega)}}, \tag{23}$$

where h_K denotes the diameter of cell K. This choice is sufficient to satisfy both the CFL condition that results from the advection of the saturation as well as from the artificial diffusion term discussed below, while our numerical experiments indicate that larger values violate these conditions.

Fig. 3 shows the size of the time steps chosen by this criterion for the two testcases considered below, and compares it with the time step chosen in the lower-order method used in [40]. We need to choose our time step smaller since we use a piecewise linear instead of the piecewise constant saturation approximation. The higher spatial order then requires a correspondingly smaller time step for stability.

3.2. Weak form and spatial discretization for the pressure/velocity part

By multiplying Eqs. (19) and (20) with test functions $\mathbf{v}$ and w respectively and then integrating terms by parts as necessary, the weak form of the problem reads: find $\mathbf{u}$, p so that for all test functions $\mathbf{v}$, w there holds

$$\left((\mathbf{K}\lambda_t(S^{(n)}))^{-1}\mathbf{u}_t^{(n+1)}, \mathbf{v}\right)_\Omega - (p^{(n+1)}, \nabla \cdot \mathbf{v})_\Omega = -(p^{(n+1)}, \mathbf{n} \cdot \mathbf{v})_{\partial\Omega}, \tag{24}$$

$$-(\nabla \cdot \mathbf{u}_t^{(n+1)}, w)_\Omega = -(q, w)_\Omega. \tag{25}$$

Here, $\mathbf{n}$ represents the unit outward normal vector to $\partial\,\Omega$ and the pressure $p^{(n+1)}$ can be prescribed weakly on the boundary $\partial\Omega$.

We use continuous finite elements to discretize the velocity and pressure equations. Specifically, we use mixed finite elements to ensure high order approximation for both vector (e.g. a fluid velocity) and scalar variables (e.g. pressure) simultaneously. For saddle point problems, it is well established that the so-called Babuska–Brezzi or Ladyzhenskaya–Babuska–Brezzi (LBB) conditions [41,38] need to be satisfied to ensure stability of the pressure-velocity system. These stability conditions are satisfied in the present work by using elements for velocity that are one order higher than for the pressure, i.e. $u_h \in Q_{p+1}^d$ and $p_h \in Q_p$, where $p = 1$, d is the space dimension, and Q_s denotes the space of tensor product Lagrange polynomials of degree s in each variable.

3.3. Stabilization, weak form and spatial discretization of the saturation transport equation

Advection problems such as the transport equation for the saturation are frequently discretized by finite volume schemes (or their more recent re-formulation in the form of discontinuous Galerkin (DG) finite element methods [38]). In contrast to this, we use continuous finite elements to discretize the saturation

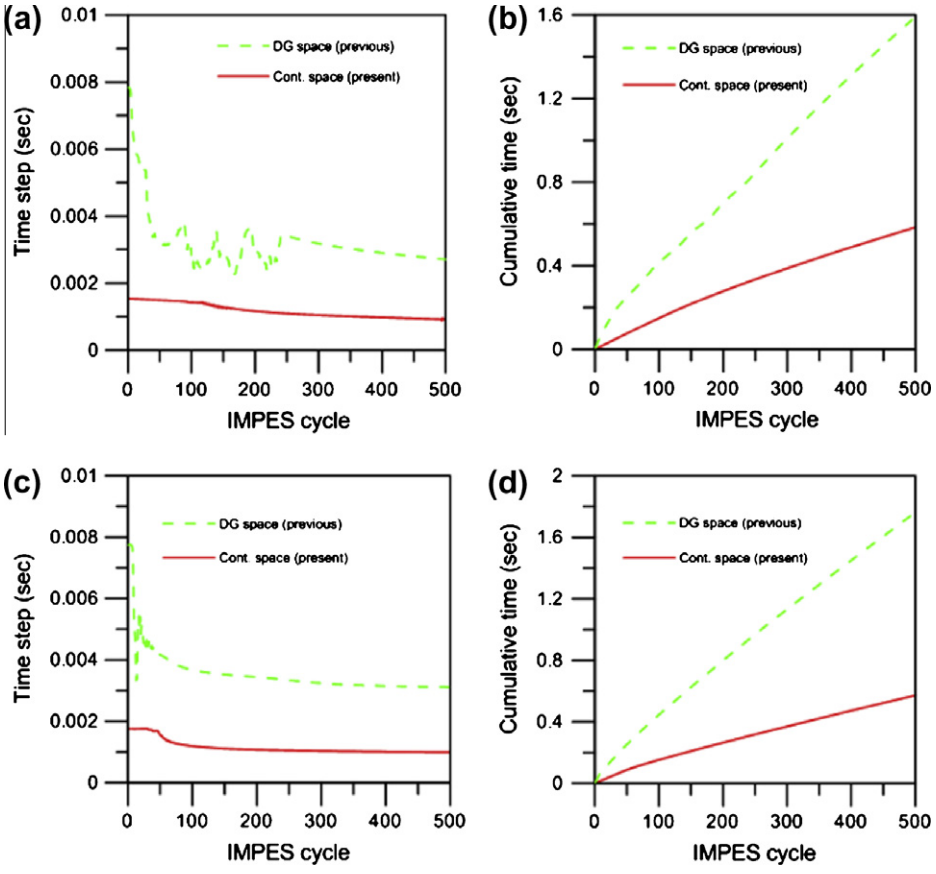

Fig. 3. Comparison of adaptive time step size between the present and previous work by Li and Bangerth [40]. (a) Time step vs. IMPES cycle for the single crack medium. (b) Cumulative time vs. IMPES cycle for the single crack medium. (c) Time step vs. IMPES cycle for the random medium. (d) Cumulative time vs. IMPES cycle for the random medium.

Author's personal copy

equation, i.e. $S_h \in Q_1$. This choice allows the simple inclusion of a capillary pressure (diffusion) term in the future: The discretization of the diffusion (Laplace) operator using DG methods leads to a significant number of additional terms that need to be integrated on each face between cells. Discontinuous Galerkin finite elements also have the drawback that the use of numerical fluxes introduces an additional numerical diffusion that acts everywhere.

These problems can be avoided using a continuous finite element space, although we still have to add some form of stabilization to make the scheme stable. We add such a stabilization in the form of a nonlinear viscosity to (22), i.e. we solve

$$\epsilon\left(\frac{S^{(n+1)}-S^{(n)}}{\Delta t^{(n+1)}}\right)+\mathbf{u}_t^{(n+1)}\cdot\nabla F(S^{(n)})-\nabla\left(v(\mathbf{u}_t^{(n+1)},S^{(a)},S^{(ex)})\nabla S^{(n)}\right) = -F(S^{(n)})q, \tag{26}$$

where $v\left(\mathbf{u}_t^{(n+1)},S^{(a)},S^{(ex)}\right)$ is the artificial viscosity, $S^{(a)}$ is an "average" saturation defined as

$$S^{(a)}=\frac{S^{(n)}+S^{(n-1)}}{2} \tag{27}$$

and $S^{(ex)}$ is an "extrapolated" saturation value given by

$$S^{(ex)}=\left(1+\frac{\Delta t^{(n)}}{\Delta t^{(n-1)}}\right)S^{(n)}-\frac{\Delta t^{(n)}}{\Delta t^{(n-1)}}S^{(n-1)}. \tag{28}$$

Note that we treat both advection as well as the artificial diffusion term explicitly in time to avoid having to re-assemble the corresponding matrices in each time step. The stabilization factor $v\left(\mathbf{u}_t^{(n+1)},S^{(a)},S^{(ex)}\right)$ is chosen in such a way that, if the discretized saturation S satisfies the original Eq. (5) exactly, the artificial diffusion term is zero. In other words, this term acts primarily in the vicinity of discontinuities in S (or other dependent variables) where in any case the numerical approximation becomes less accurate, but does not affect the areas where the saturation varies smoothly and the numerical approximation is accurate. The literature contains a number of approaches to achieve this. Here we adopt a scheme developed by Guermond and Pasquetti [39] which builds on a suitably defined residual and a limiting procedure for the additional viscosity. The artificial viscosity is a piecewise constant function defined on each cell K with diameter h_K as

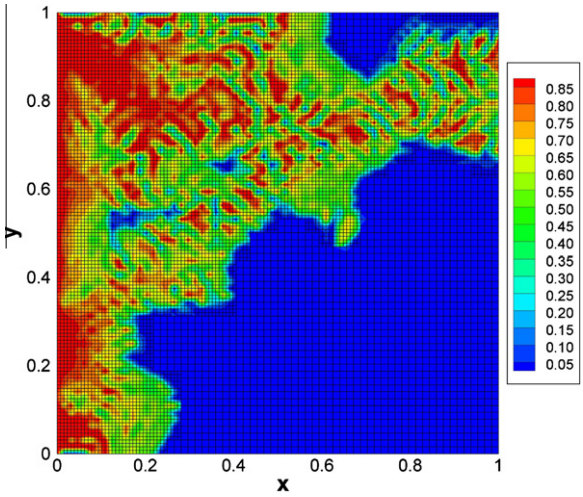

Fig. 4. Spurious oscillations in the saturation solution for the random media case in the absence of a stabilization term.

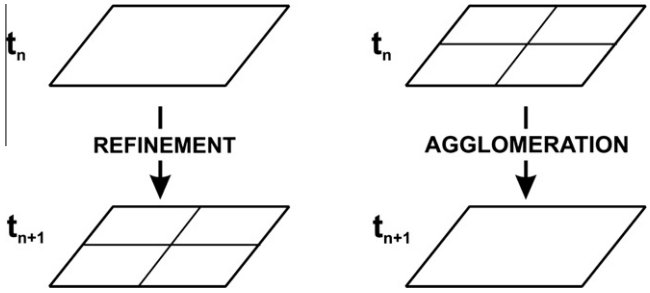

Fig. 5. Illustration of local mesh adaptation process.

$$v\left(\mathbf{u}_t^{(n+1)},S^{(a)},S^{(ex)}\right)|_K=\beta\|\mathbf{u}_t^{(n+1)}\|_{L^\infty(K)} \times\min\left\{h_K,h_K^\alpha\frac{\|\mathrm{Res}\left(\mathbf{u}_t^{(n+1)},S^{(a)}\right)\|_{L^\infty(K)}}{c\left(\mathbf{u}_t^{(n+1)},S^{(ex)}\right)}\right\} \tag{29}$$

where α is a stabilization exponent that we chose to be $\alpha = 1$, and β is a user-defined dimensionless stabilization constant that is chosen

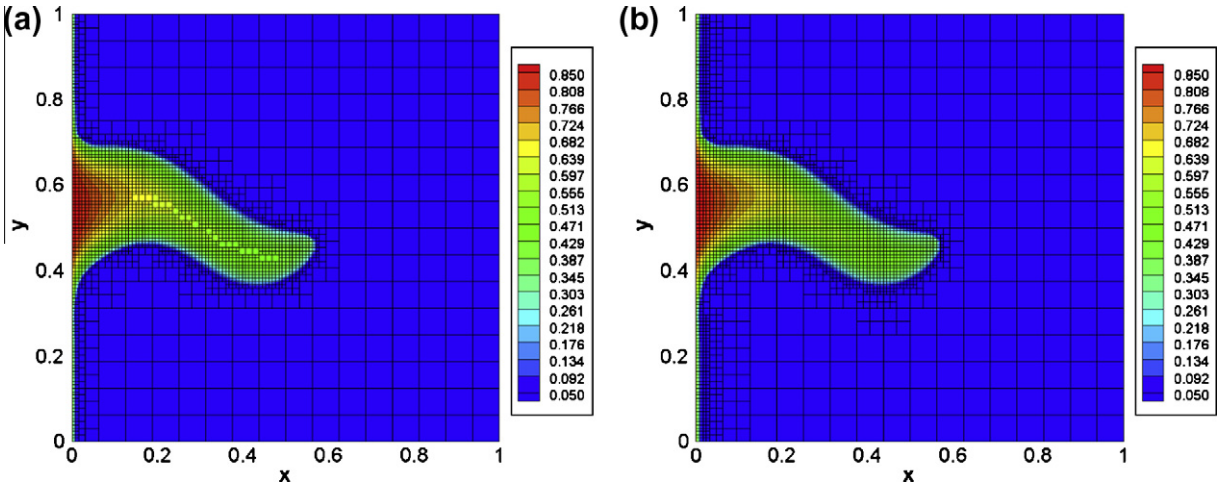

Fig. 6. Effect of refinement indicator threshold: saturation field and adaptive mesh for single crack medium at $t = 0.359$ s. (a) Cells are coarsened if $\eta_K < 1.1$ and refined if $\eta_K > 1.7$ (2608 computational cells). (b) Threshold values for coarsening and refinement are chosen as 0.21 and 0.28 (2938 computational cells).

Author's personal copy

as small as possible but as large as necessary to avoid unphysical oscillations in the solution. Following Guermond and Pasquetti [39] as well as Kronbichler and Bangerth [44], the velocity and saturation global normalization constant, $c\left(\mathbf{u}_t^{(n+1)}, S^{(ex)}\right)$, and the residual $\mathrm{Res}\left(\mathbf{u}_t^{(n+1)}, S^{(a)}\right)$ are given by

$$c\left(\mathbf{u}_t^{(n+1)}, S^{(ex)}\right) = c_R \|\mathbf{u}_t^{(n+1)}\|_{L^\infty(\Omega)} \mathrm{var}(S^{(ex)}) |\mathrm{diam}(\Omega)|^{\alpha-2}, \tag{30}$$

$$\mathrm{Res}\left(\mathbf{u}_t^{(n+1)}, S^{(a)}\right) = \left(\epsilon\left(\frac{S^{(n)} - S^{(n-1)}}{\Delta t^{(n)}}\right) + \mathbf{u}_t^{(n+1)} \cdot \nabla F\left(S^{(a)}\right) + (S^{(a)})q\right) \cdot (S^{(a)})^{\alpha-1}, \tag{31}$$

where c_R is a dimensionless user-defined normalization constant, $\mathrm{diam}(\Omega)$ is the diameter of the domain and $\mathrm{var}(S^{(ex)})$ is the range of the extrapolated saturation values in the entire computational domain Ω, given mathematically by

$$\mathrm{var}(S^{(ex)}) = \max_\Omega S^{(ex)} - \min_\Omega S^{(ex)}. \tag{32}$$

Table 1
Parameters used in the model

Parameter	Symbol	Value	Units
Porosity	ϵ	1.0	–
Viscosity (wetting)	μ_w	0.2	kg m^{-1} s^{-1}
Viscosity (non-wetting)	μ_{nw}	1.0	kg m^{-1} s^{-1}
Stabilization exponent	α	1.0	–
Stabilization constant	β	0.4	–
Normalization constant	c_R	1.0	–

Guermond and Pasquetti [39] demonstrate excellent performance and computational results for this scheme and provide details on the derivation. The stabilization term is critical in order to obtain a saturation field that is oscillation free. Spurious oscillations that occur without the stabilization term are illustrated in Fig. 4. Results discussed subsequently using the above method are free of such unphysical oscillations.

With the artificial diffusion term defined as above, we obtain the weak form of our discrete equations by multiplying Eq. (26) with a test function σ and integrating by parts as necessary. We then obtain

$$\begin{aligned}(\epsilon S^{(n+1)}, \sigma)_\Omega - \Delta t^{(n+1)}\left(F(S^{(n)})\mathbf{u}_t^{(n+1)}, \nabla\sigma\right)_\Omega + \Delta t^{(n+1)}\left(F\left(S^{(n)}\right)\left(\mathbf{n}\cdot\mathbf{u}_t^{(n+1)}\right), \sigma\right)_{\partial\Omega} \\ = (\epsilon S^{(n)}, \sigma)_\Omega - \Delta t^{(n+1)}\left(\nu\left(\mathbf{u}_t^{(n+1)}, S^{(a)}, S^{(ex)}\right)\nabla S^{(n)}, \nabla\sigma\right)_\Omega \\ + \Delta t^{(n+1)}\left(\mathbf{n}\cdot\nu\left(\mathbf{u}_t^{(n+1)}, S^{(a)}, S^{(ex)}\right)\nabla S^{(n)}, \sigma\right)_{\partial\Omega}.\end{aligned} \tag{33}$$

In Eq. (33), there are two boundary integral terms corresponding to Dirichlet and Neumann boundary conditions. In the present work, we require only Dirichlet boundary conditions for saturation,

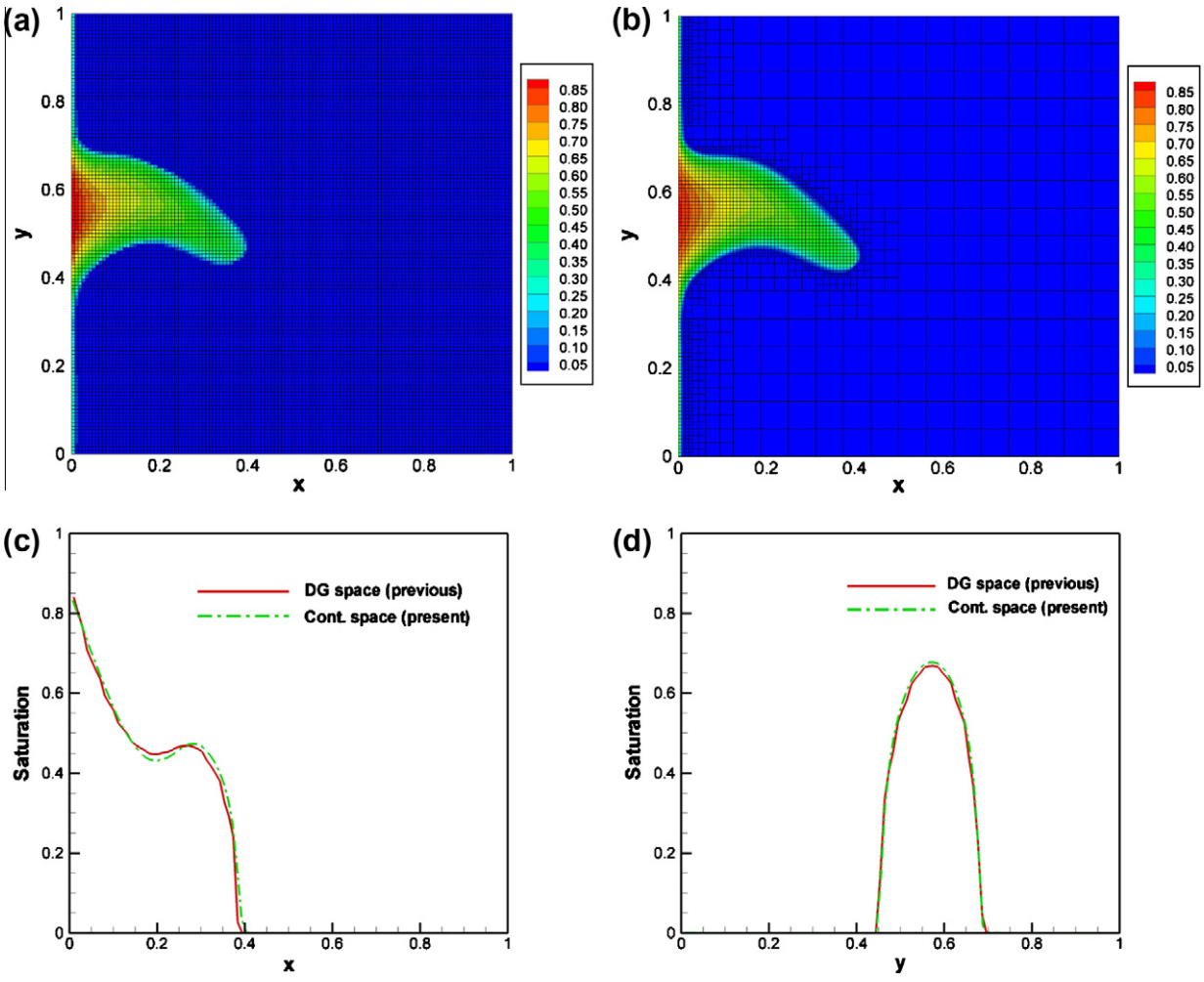

Fig. 7. Numerical results for the single crack medium in comparison with previous work of Li and Bangerth [40] at $t = 0.154$ s. (a) Saturation field using discontinuous Galerkin space (previous work). (b) Saturation field using continuous space with the stabilized term (present work). (c) Saturation profile along $y = 0.5$ (d) Saturation profile along $x = 0.1$.

Author's personal copy

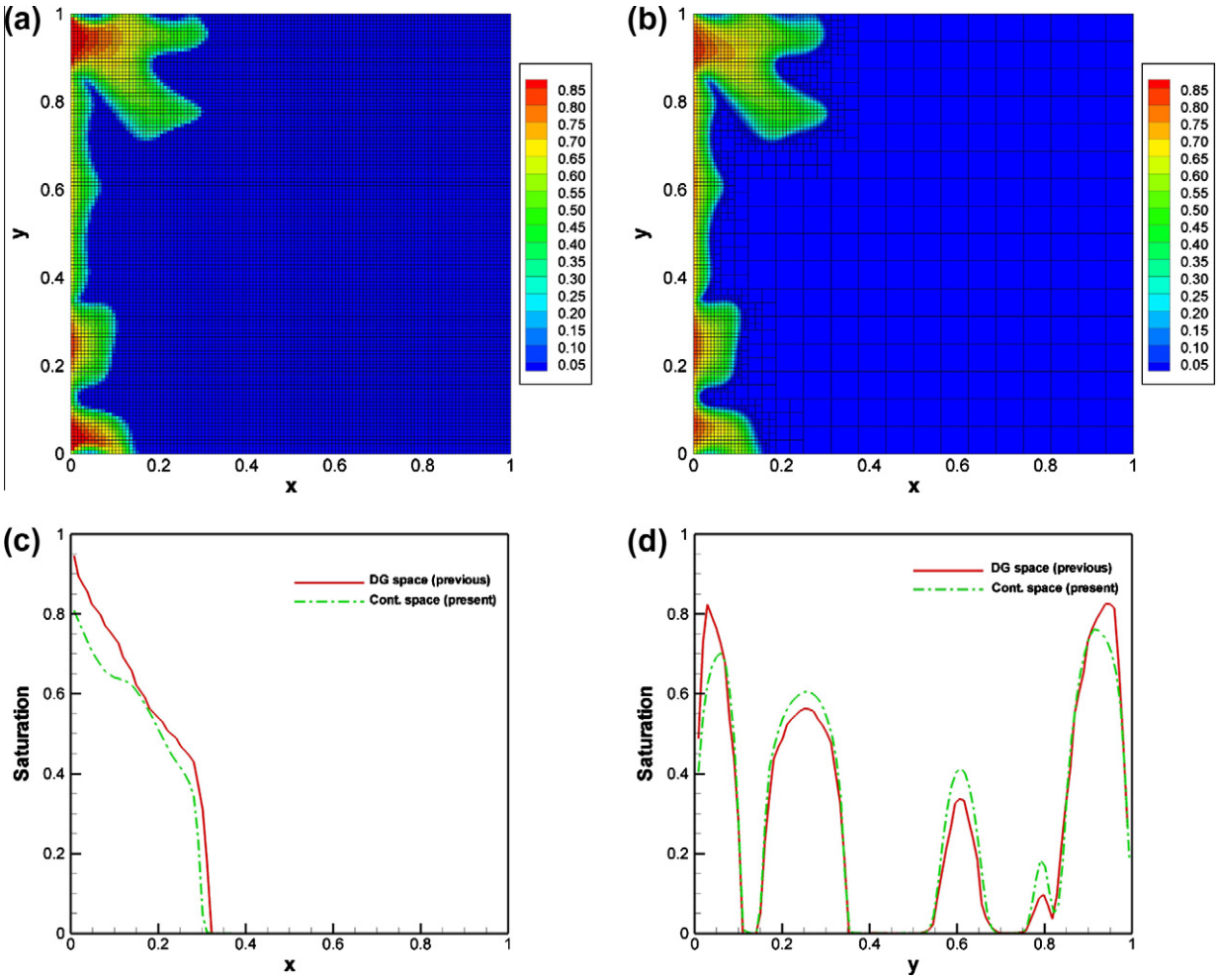

Fig. 8. Numerical results for the random medium in comparison with previous work of Li and Bangerth [40] at $t = 0.249$ s. (a) Saturation field using discontinuous Galerkin space (previous work). (b) Saturation field using continuous space with the stabilized term (present work). (c) Saturation profile along $y = 0.95$. (d) Saturation profile along $x = 0.05$.

as is described in Section 2.2, and therefore the Neumann boundary integral term vanishes.

Since the Dirichlet boundary conditions for saturation are only imposed on the inflow boundaries, the third term on the left hand side of Eq. (33) needs to be split further into two parts:

$$\Delta t^{(n+1)}\left(F(S^{(n)})\left(\mathbf{n}\cdot\mathbf{u}_t^{(n+1)}\right),\sigma\right)_{\partial\Omega} = \Delta t^{(n+1)}\left(F\left(S_{(+)}^{(n)}\right)\left(\mathbf{n}\cdot\mathbf{u}_{t(+)}^{(n+1)}\right),\sigma\right)_{\partial\Omega_{(+)}} + \Delta t^{(n+1)}\left(F\left(S_{(-)}^{(n)}\right)\left(\mathbf{n}\cdot\mathbf{u}_{t(-)}^{(n+1)}\right),\sigma\right)_{\partial\Omega_{(-)}}, \tag{34}$$

where $\partial\Omega_{(-)} = \{\mathbf{x}\in\partial\Omega : \mathbf{n}\cdot\mathbf{u}_t < 0\}$ and $\partial\Omega_{(+)} = \{\mathbf{x}\in\partial\Omega : \mathbf{n}\cdot\mathbf{u}_t > 0\}$ represent inflow and outflow boundaries, respectively. We choose values using an upwind formulation, i.e. $S_{(+)}^{(n)}$ and $\mathbf{u}_{t(+)}^{(n+1)}$ correspond to the values taken from the present cell, while the values of $S_{(-)}^{(n)}$ and $\mathbf{u}_{t(-)}^{(n+1)}$ are those taken from the neighboring boundary $\partial\Omega_{(-)}$.

3.4. Linear system

Discretization of Eqs. (24), (25) and (33) yields the following linear system that needs to be solved for time step $n+1$:

$$\begin{pmatrix}\mathbf{M}^{\mathbf{u}} & \mathbf{B}^T & \mathbf{0}\\ \mathbf{B} & \mathbf{0} & \mathbf{0}\\ \mathbf{H} & \mathbf{0} & \mathbf{M}^S\end{pmatrix}\begin{pmatrix}\mathbf{U}^{(n+1)}\\ \mathbf{P}^{(n+1)}\\ \mathbf{S}^{(n+1)}\end{pmatrix} = \begin{pmatrix}0\\ \mathbf{F}_2\\ \mathbf{F}_3\end{pmatrix}, \tag{35}$$

where the individual matrices and vectors are defined as follows using shape functions $\mathbf{v}_i$ for velocity, and ϕ_i for both pressure and saturation:

$$\mathbf{M}^{\mathbf{u}}_{ij} = ((\mathbf{K}\lambda_t(S^{(n)}))^{-1}\mathbf{v}_i,\mathbf{v}_j)_\Omega, \quad \mathbf{M}^S_{ij} = (\epsilon\phi_i,\phi_j)_\Omega, \tag{36}$$

$$\mathbf{B}_{ij} = -(\nabla\cdot\mathbf{v}_j,\phi_i)_\Omega, \mathbf{H}_{ij} = -\Delta t^{(n+1)}(F(S^{(n)})\mathbf{v}_i,\nabla\phi_j)_\Omega, \tag{37}$$

$$(\mathbf{F}_2)_i = -(F(S^{(n)})q,\phi_i)_\Omega, \tag{38}$$

and

$$(\mathbf{F}_3)_i = (\epsilon S^{(n)},\phi_i)_\Omega - \Delta t^{(n+1)}(v(\mathbf{u}_t^{(n+1)},S^{(a)},S^{(ex)})\nabla S^{(n)},\nabla\phi_i)_\Omega \tag{39}$$

We will solve these equations by first computing the updated pressures $\mathbf{P}^{(n+1)}$ and then the velocities $\mathbf{U}^{(n+1)}$. The final step is to solve for updated saturation $\mathbf{S}^{(n+1)}$. To this end, we can form the Schur complement (i.e., do a block elimination, see [45]) of the top left 2×2 block of the matrix to obtain

$$\mathbf{B}(\mathbf{M}^{\mathbf{u}})^{-1}\mathbf{B}^T\mathbf{P}^{(n+1)} = -\mathbf{F}_2, \tag{40}$$

$$(\mathbf{M}^{\mathbf{u}})\mathbf{U}^{(n+1)} = -\mathbf{B}^T\mathbf{P}^{(n+1)}. \tag{41}$$

We can therefore obtain the pressure and velocity solution by first inverting the Schur complement matrix $\mathbf{S} = \mathbf{B}(\mathbf{M}^{\mathbf{u}})^{-1}\mathbf{B}^T$ and next the mass matrix $\mathbf{M}^{\mathbf{u}}$ on the velocity space. Both matrices are symmetric and positive definite and therefore amenable to the

Author's personal copy

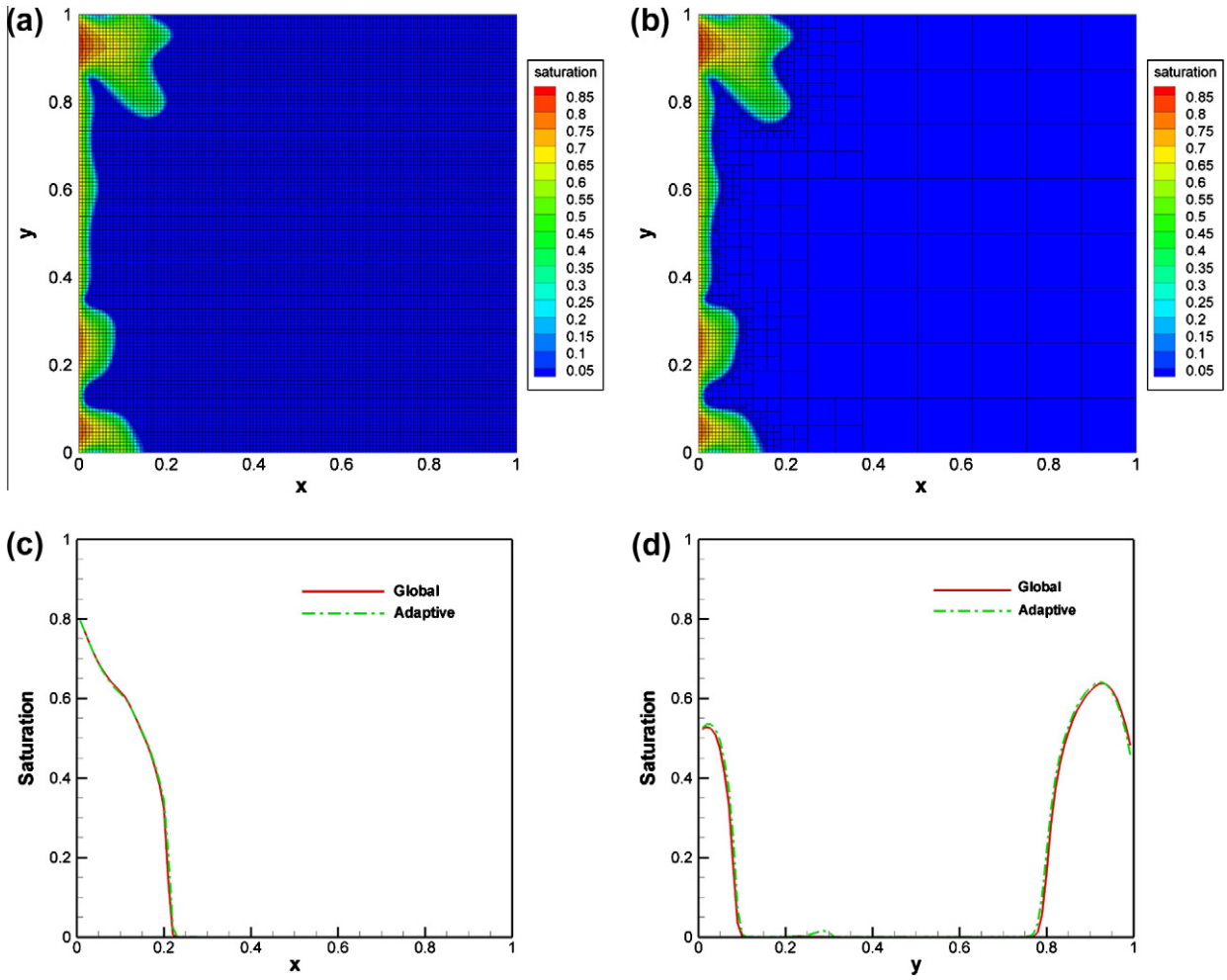

Fig. 9. Comparison of computational mesh distribution and saturation fields at $t = 0.278$ s using the continuous discretization. (a) Uniform mesh with 16,384 elements and 165,380 degrees of freedom. (b) Adaptive mesh with 1981 elements and 7924 degrees of freedom. (c) Saturation profile along $y = 0.95$. (d) Saturation profile along $x = 0.15$.

conjugate gradient method. There are various strategies to precondition the Schur complement solve, using the fact that $\mathbf{S}$ is a discrete representation of the Laplace operator. We choose to precondition with $\widetilde{\mathbf{S}}^{-1} = [\mathbf{B}(\mathrm{diag}\mathbf{M}^{\mathbf{u}})^{-1}\mathbf{B}^T]^{-1}$ since $\widetilde{\mathbf{S}}$ is a matrix that is cheap to apply and therefore significantly simpler to invert than $\mathbf{S}$. At the same time, the preconditioned matrix $\widetilde{\mathbf{S}}^{-1}\mathbf{S}$ has a nearly constant condition number and can consequently be solved in a constant number of iterations, irrespective of the refinement level [46]. An alternative is to precondition with an (approximate) inverse of a matrix obtained from a primal (non-mixed) discretization of the Laplace operator.

Once the velocity is available, we can assemble $\mathbf{H}$ and $\mathbf{F}_3$ (which depend on $\mathbf{u}^{(n+1)}$ implicitly) and solve for the saturations as

$$\mathbf{M}^S\mathbf{S}^{(n+1)} = \mathbf{F}_3 - \mathbf{H}\mathbf{U}^{(n+1)}. \tag{42}$$

4. Adaptive mesh refinement strategy

In analogy with widely used schemes in compressible flow problems, the adaptive refinement technique adopted here is based upon the transient saturation gradient. Once a solution $S^{(n)}$ is computed on a given mesh, we compute a refinement indicator

$$\eta_K = |\nabla S_p^{(n+1)}(\mathbf{x}_K)| \tag{43}$$

where $\mathbf{x}_K$ is the cell center. Here,

$$S_p^{(n+1)} = S^{(n)} + \Delta t^{(n+1)}\frac{S^{(n)} - S^{(n-1)}}{\Delta t^{(n+1)}} = 2S^{(n)} - S^{(n-1)} \tag{44}$$

is a predictor for the saturation profile in the next time step. We choose a predicted saturation profile for our refinement indicator since the mesh so created will be used to discretize future time steps, not the current one: we want to refine ahead of a front, rather than propagating into a coarse set of elements and thereby smearing the saturation solutions.

With the refinement indicators η_K so defined, refinement proceeds along the following algorithm [33,42]:

(1) If η_K is larger than a threshold θ_r, then mark the cell K for refinement if the resulting children will not exceed the chosen maximum refinement level.
(2) If η_K is smaller than a threshold θ_c, then mark the cell K for coarsening if the resulting cell is not coarser than the initial mesh.
(3) If for a non-active cell not all children are marked for coarsening, then remove coarsening flags from all children.
(4) Mark additional cells for refinement to ensure that the resulting mesh has no interfaces between cells that differ in refinement by more than one level.
(5) Refine and coarsen all cells marked as above.

This adaptive procedure is illustrated graphically in Fig. 5.

Author's personal copy

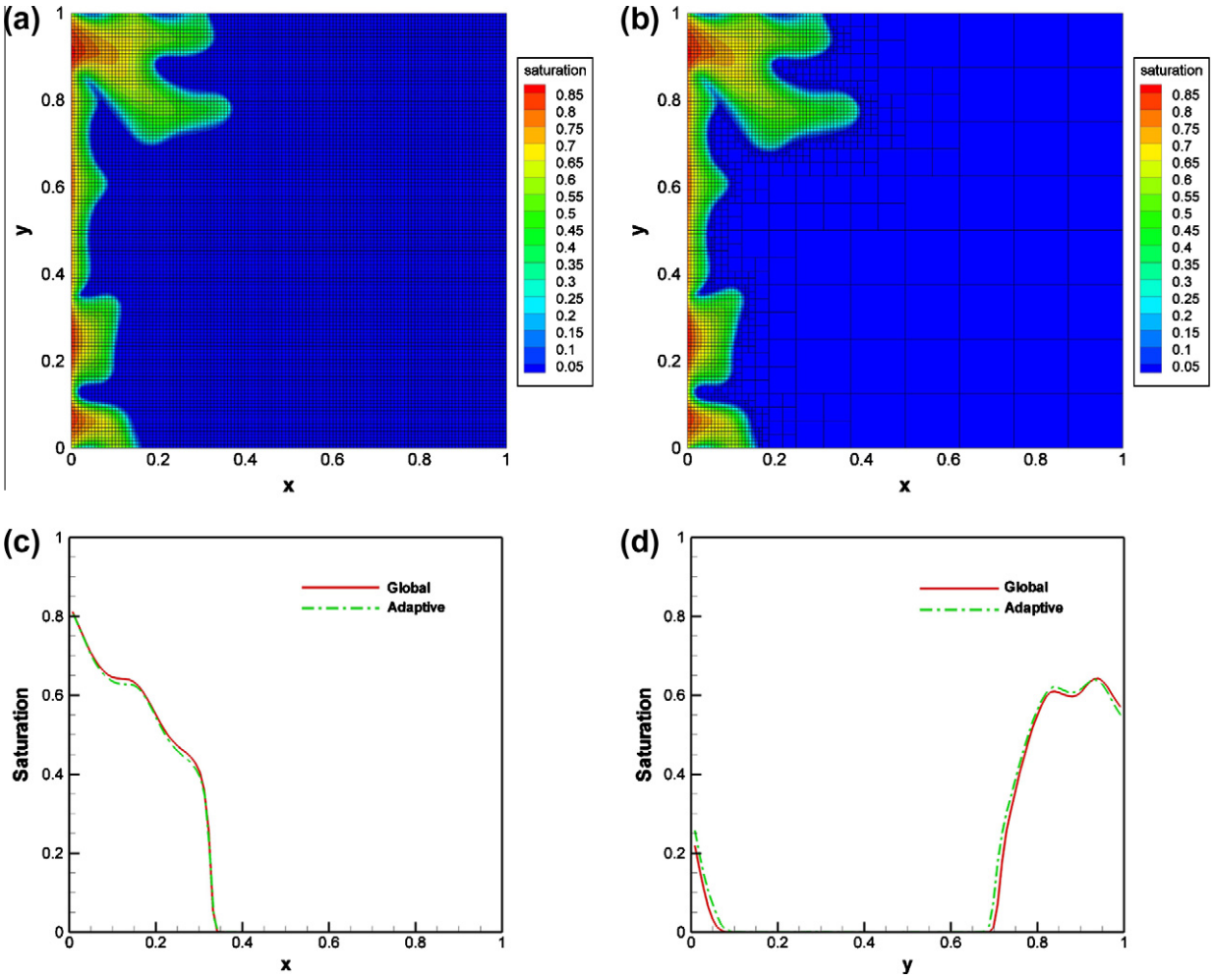

Fig. 10. Comparison of computational mesh distribution and saturation fields at $t = 0.488$ s using the continuous discretization. (a) Uniform mesh with 16,384 elements and 165,380 degrees of freedom. (b) Adaptive mesh with 3220 elements and 12,880 degrees of freedom. (c) Saturation profile along $y = 0.95$. (d) Saturation profile along $x = 0.15$.

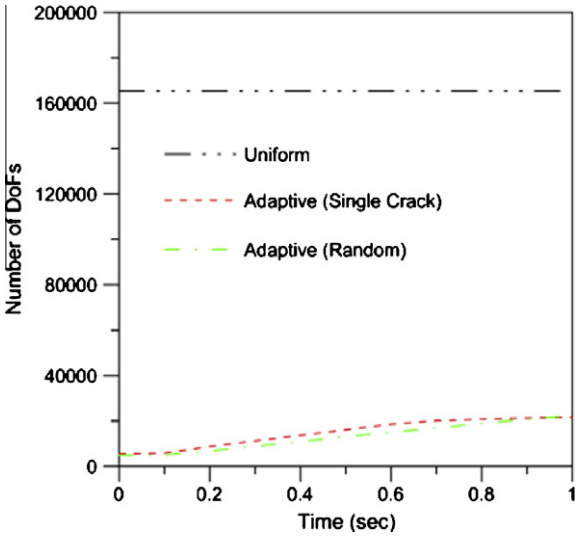

Fig. 11. Comparison of the number of degrees of freedom in the single crack and random media cases with the corresponding number for uniform grids. The adaptive meshes need between 86% and 96% fewer degrees of freedom.

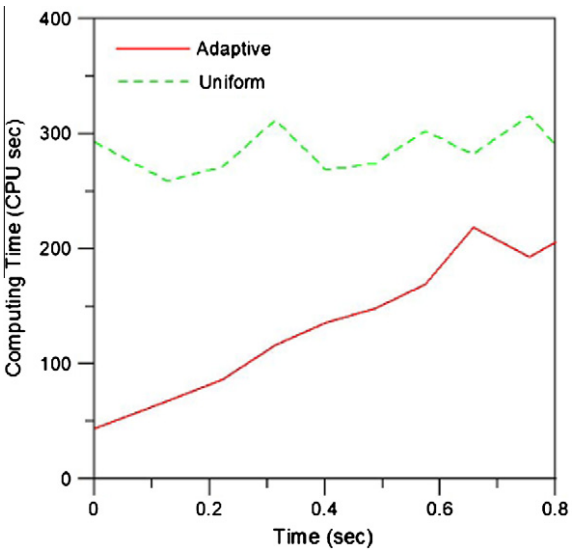

Fig. 12. CPU time per IMPES step for the adaptive and uniform grid simulations.

To illustrate the effect of selecting different threshold levels, results obtained for two simulations under otherwise identical conditions are shown in Fig. 6. In the first simulation, cells are coarsened if $\eta_K < \theta_c = 1.1$ and refined if $\eta_K > \theta_r = 1.7$. In the second, these thresholds are chosen as $\theta_c = 0.21$ and $\theta_r = 0.28$. As can be seen, the saturation fields are essentially identical, but the less stringent, first set of threshold values result in more coarsening,

Author's personal copy

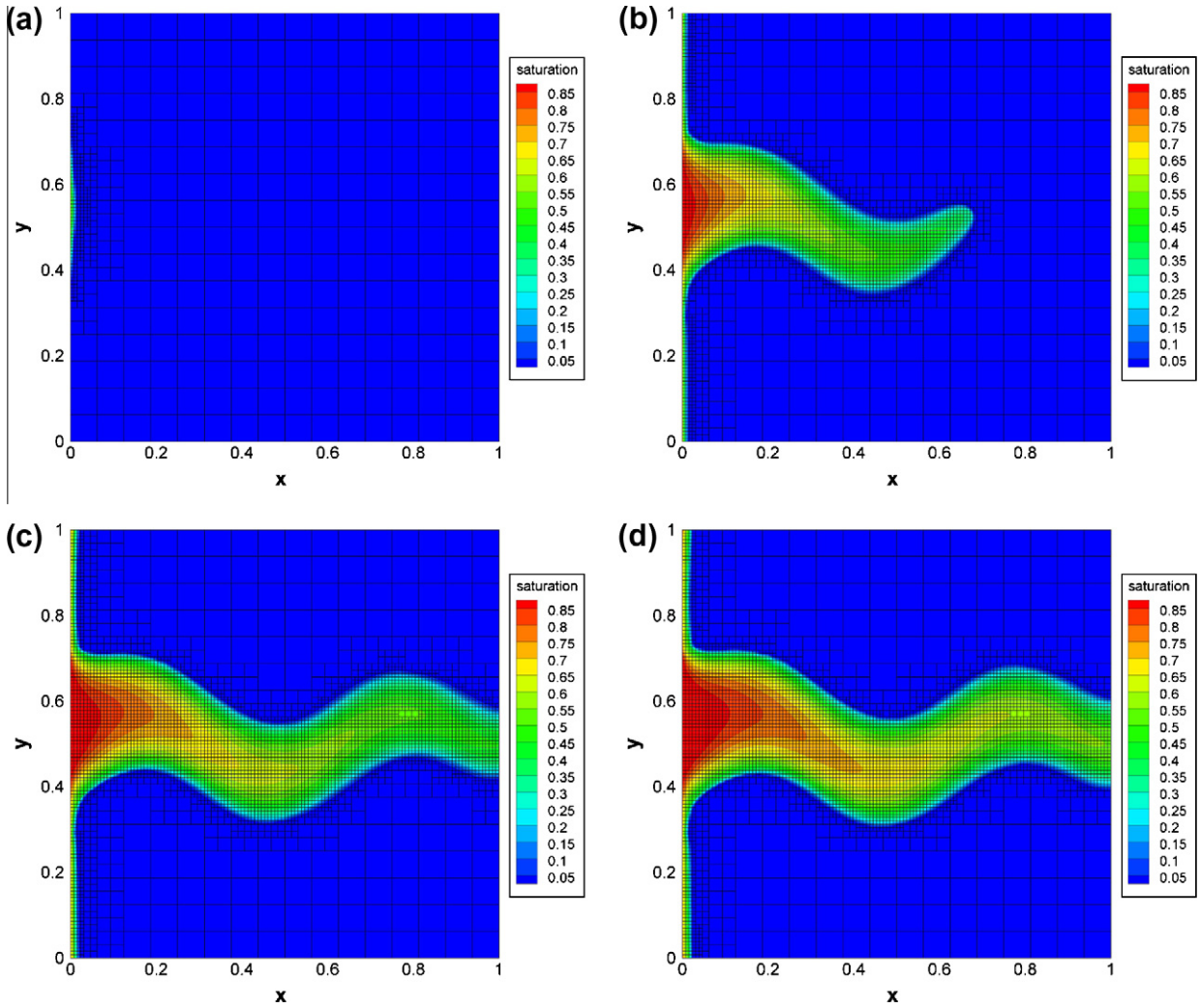

Fig. 13. Saturation fields for the single crack medium. (a) $t = 0.002$ s with 520 elements and 2080 degrees of freedom. (b) $t = 0.427$ s with 3424 elements and 13,696 degrees of freedom. (c) $t = 0.731$ s with 5185 elements and 20,740 degrees of freedom. (d) $t = 0.979$ s with 5551 elements and 22,204 degrees of freedom.

particularly along the center of the crack as well as along the inlet boundary. This yields a computational mesh with about 12% less cells. To ensure high accuracy, all following computations were done with the second set of thresholds, however.

5. Results and discussion

The simulations presented and analyzed in this section were performed using the spatial permeability distributions given in Section 2.1, and with the input parameters listed in Table 1. It should be noted that in the validation section, the porosity is set to 0.6 rather than the value of 1.0 used in all other cases. Our implementation uses the Open Source finite element library deal.II [42] written in C++.

5.1. Numerical validation

Here, for numerical validation, we compare the present results obtained with the adaptive grid method to previous work using uniform grids in which Raviart–Thomas finite elements are adopted for velocity and discontinuous Galerkin (DG) elements for pressure and saturation [40].

Fig. 7a and b compares saturation contours in the single crack case between these two discretizations at $t = 0.154$ s in the single crack case. Fig. 7c and d shows saturation profiles along $y = 0.5$ and $x = 0.1$, respectively. The results are essentially identical.

In the case of a random medium, there are a couple of small but more noticeable differences as shown in the results at $t = 0.249$ s presented in Fig. 8. The extent of the penetration of the invading fluid is predicted to be higher in the DG simulations (see top and bottom fingers in Fig. 8a), and there are differences of up to 10% in the saturation as shown in both the longitudinal and transverse profiled in Fig. 8c and d. These differences are due to the lower accuracy and higher diffusivity of the low-order DG approximation. In contrast, the discretization used here shows a more pronounced and less diffused appearance, a consequence of the less heavy-handed stabilization even though we use far fewer degrees of freedom compared to the uniformly refined grid used for the DG method.

5.2. Comparison of global vs. adaptive refinement

Figs. 9 and 10 show the saturation distribution in the random medium obtained using global and locally adaptive refinement at $t = 0.278$ s and $t = 0.488$ s respectively. Well resolved saturation distributions that are quasi-identical can be obtained using both refinement techniques. The effectiveness of the adaptive grid method is highlighted by the fact that, at time $t = 0.278$ s for instance (Fig. 9), only 7924 degrees of freedom (DoFs) are required

Author's personal copy

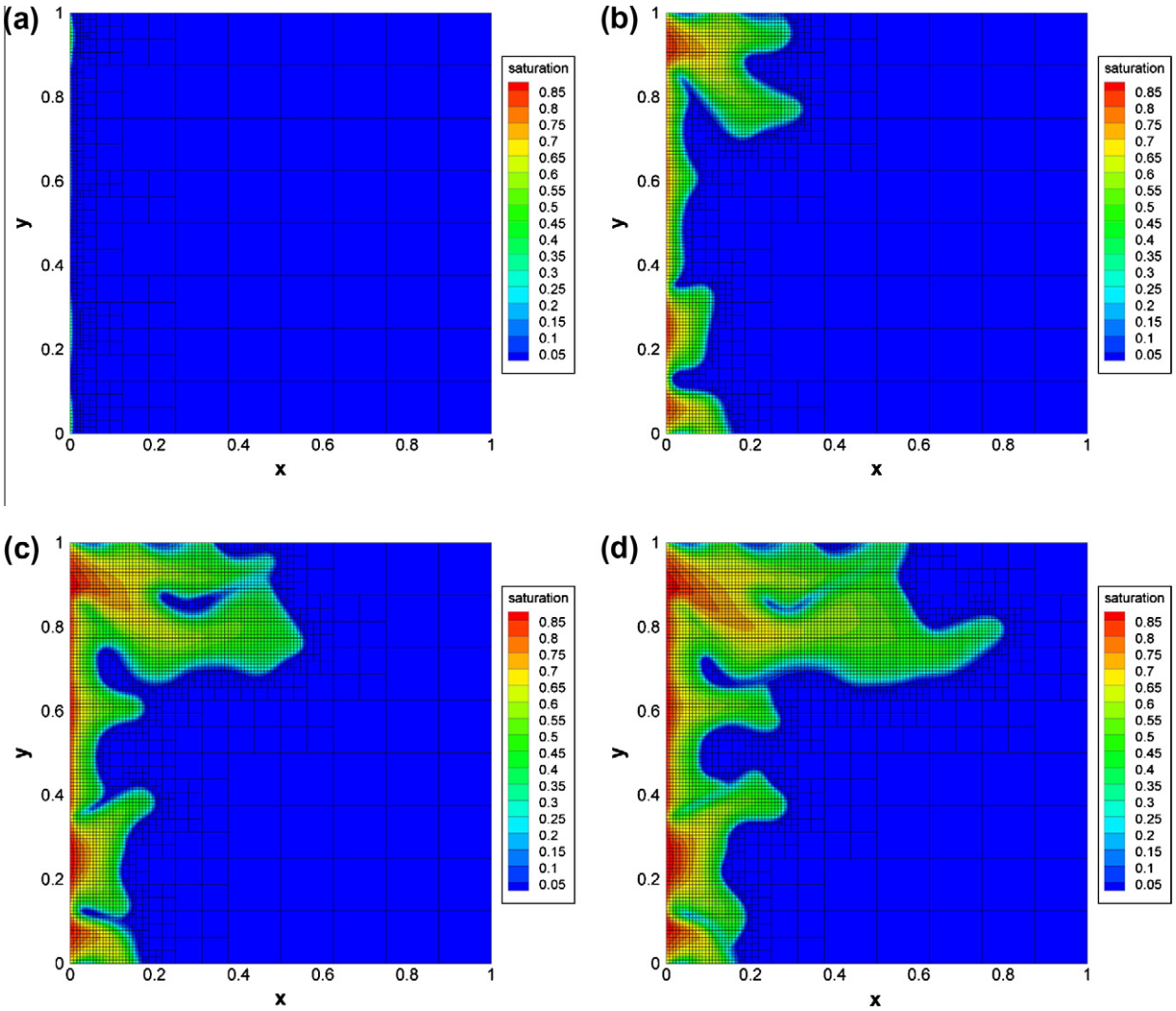

Fig. 14. Saturation fields for the random medium. (a) $t = 0.003$ s with 544 elements and 2176 degrees of freedom. (b) $t = 0.411$ s with 2722 elements and 10,888 degrees of freedom. (c) $t = 0.755$ s with 4744 elements and 18,976 degrees of freedom. (d) $t = 1.085$ s with 6361 elements and 25,444 degrees of freedom.

with local adaptation compared to 165,380 DoFs for the globally refined uniform grid. The total number of degrees of freedom for the local adaptive method increases with time: as the wetting phase (water) gradually invades the areas initially occupied by the non-wetting phase (oil) a correspondingly larger part of the computational domain is refined. As the gradients abate in the water invaded portion of the domain, the mesh is coarsened again. Overall, the required number of DoFs was reduced by 86 to 96% ($t = 0$ and $t = 1$) for both single crack and random media as shown in Fig. 11. Fig. 12 compares the computing (CPU) time per IMPES step as a function of the process simulation time; significant computational performance gains are achieved with the locally adaptive method, resulting in an overall reduction of the aggregate CPU time for the entire simulation of 42% without any reduction in accuracy in the solution. Experience shows that the savings in both number of unknowns as well as CPU time would be even larger for three dimensional simulations.

5.3. Saturation distribution in a domain with a single crack

Having established the accuracy of the adaptive mesh two-phase flow method, further analysis of the single crack simulations with the permeability given by Eq. (12) are presented here. Such simulations can be considered an idealized representation of situations arising in fuel cell fibrous media when carbon fibres break due to over-compression [47–49]; in geo-science, a porous medium with a single crack distribution can be found in sandstone reservoir rocks [5,2].

The saturation distribution as a function of time is shown in Fig. 13. The mobile fluid slowly meanders its way along the central areas where permeability is highest. In this case, due to the higher saturation gradients in the central area, locally refined cells are concentrated in the middle of the domain and propagate in time with the saturation front.

5.4. Saturation distribution in a porous medium with random permeability

Simulations presented in this section were performed for a medium with a permeability distribution given by Eq. (13), see Fig. 2. The saturation distribution is shown in Fig. 14. Fig. 14b shows that the more mobile displacing fluid seeks pathways formed by inter-connected high-permeability zones, faults and fractures. The fluid appears to form fingers, a phenomenon frequently found in both oil reservoirs and also reported in porous diffusion media of fuel cells [50].

Author's personal copy

6. Conclusions and future work

A numerical method allowing high resolution simulations of two-phase flow in porous media was presented. The method is based on a finite element discretization using continuous elements. It incorporates a new entropy based stabilizing term that ensures accuracy while providing stability, and locally adaptive refinement allowing highly resolved time dependent simulations. The effectiveness of the numerical method was demonstrated by performing simulations corresponding to two-phase flow in two types of porous media (single crack and heterogeneous).

The implementation used an implicit pressure and explicit saturation (IMPES) formulation. Compared to a simple finite volume (or DG scheme), the higher order of approximation used for the saturation variable, in conjunction with the stabilizing dissipative term, makes the standard CFL restriction (i.e. $\Delta t \leqslant h/|\mathbf{u}|$) no longer suitable for evaluating the adaptive time step for the modified Eq. (26). In order to further improve computational efficiency, future work will focus on the development and implementation of more efficient time stepping schemes, and a particularly attractive avenue is the use of an adaptive time stepping strategy that takes advantage of the slower variation of pressure compared to saturation [29,30], and allows larger time steps for the computationally costly pressure equation. Such an algorithm would make it more practical to perform 3D simulations including enhanced physical modelling, such as capillary diffusion, that would enhance the applicability of the method to a broader range of multi-phase transport problems of practical interest.

Acknowledgments

The work of the first, second and fourth authors was funded through the Canada Research Chairs Program and the MITACS Network of Centres of Excellence. Parts of the work by the third author (WB) were funded through Award No. KUS-C1-016-04, made by the King Abdullah University of Science and Technology, and through an Alfred P. Sloan Research Fellowship.

Thanks are due to Dr. Zhangxin Chen (University of Calgary) for his invaluable insights on finite element theory and to Mrs. Hsiao-Yun Janette Cheng (PhD candidate, University of Sheffield), for helping with the graphics.

References

[1] Bear J. Dynamics of fluids in porous media. American Elsevier; 1972.
[2] Nield DA, Bejan A. Convection in porous media. New York: Springer; 2006.
[3] Peaceman DW. Fundamentals of numerical reservoir simulation. Amsterdam: Elsevier; 1977.
[4] Aziz K, Settari A. Petroleum reservoir simulation. London: Applied Science Publishers Ltd.; 1979.
[5] Gerritsen MG, Durlofsky LJ. Modeling fluid flow in oil reservoirs. Annu Rev Fluid Mech 2005;37(1):211–38.
[6] Branets LV, Ghai SS, Lyons SL, Wu XH. Challenges and technologies in reservoir modeling. Commun Computat Phys 2009;6(1):1–23.
[7] Lister S, Djilali N. Two-phase transport in porous gas diffusion electrodes. In: Faghri M, Sunden B, editors. Southampton (UK): WIT Press; 2005.
[8] Djilali N. Computational modelling of polymer electrolyte membrane (PEM) fuel cells: challenges and opportunities. Energy 2007;32(4):269–80.
[9] Djilali N, Sui PC. Transport phenomena in fuel cells: from microscale to macroscale. Int J Computat Fluid Dynam 2008;22(1–2):115–33.
[10] Kumbur EC, Sharp KV, Mench MM. Validated Leverett approach for multiphase flow in PEFC diffusion media. J Electrochem Soc 2007;154(12):B1295–304.
[11] Kumbur EC, Sharp KV, Mench MM. Validated Leverett approach for multiphase flow in PEFC diffusion media. J Electrochem Soc 2007;154(12):B1305–14.
[12] Kumbur EC, Sharp KV, Mench MM. Validated Leverett approach for multiphase flow in PEFC diffusion media. J Electrochem Soc 2007;154(12):B1315–24.
[13] Niessner J, Helmig R. Multi-scale modeling of three-phase-three-component processes in heterogeneous porous media. Adv Water Resour 2007;30(11):2309–25.
[14] Niessner J, Helmig R, Jakobs H, Roberts JE. Interface condition and linearization schemes in the newton iterations for two-phase flow in heterogeneous porous media. Adv Water Resour 2005;28(7):671–87.
[15] Kees CE, Miller CT. Higher order time integration methods for two-phase flow. Adv Water Resour 2002;25(2):159–77.
[16] Binning P, Celia MA. Practical implementation of the fractional flow approach to multi-phase flow simulation. Adv Water Resour 1999;22(5):461–78.
[17] Tseng PH, Zyvoloski GA. A reduced degree of freedom method for simulating non-isothermal multi-phase flow in a porous medium. Adv Water Resour 2000;23(7):731–45.
[18] Piri M, Blunt MJ. Three-dimensional mixed-wet random pore-scale network modeling of two- and three-phase flow in porous media. I. Model description. Phys Rev E 2005;71(2):026301.
[19] Christov I, Popov B. New non-oscillatory central schemes on unstructured triangulations for hyperbolic systems of conservation laws. J Computat Phys 2008;227(11):5736–57.
[20] Hou T, Wu XH. A multiscale finite element method for elliptic problems in composite materials and porous media. J Computat Phys 1997;134(1):169–89.
[21] Durlofsky LJ, Efendiev Y, Ginting V. An adaptive local–global multiscale finite volume element method for two-phase flow simulations. Adv Water Resour 2007;30(3):576–88.
[22] Efendiev Y, Ginting V, Hou T, Ewing R. Accurate multiscale finite element methods for two-phase flow simulations. J Computat Phys 2006;220(1):155–74.
[23] Efendiev Y, Hou T. Multiscale finite element methods for porous media flows and their applications. Appl Numer Math 2007;57(5-7):577–96.
[24] Jenny P, Lee SH, Tchelepi HA. Multi-scale finite-volume method for elliptic problems in subsurface flow simulation. J Computat Phys 2003;187(1):47–67.
[25] Helmig R, Niessner J, Class H. Recent advances in finite element methods for multi-phase flow processes in porous media. Int J Computat Fluid Dynam 2006;20(3/4):245–52.
[26] Sheldon JW, Zondek B, Cardwell WT. One-dimensional, incompressible, non-capillary, two-phase fluid flow in a porous medium. Trans SPE AIME 1959;216:290–6.
[27] Stone HL, Garder Jr. Analysis of gas-cap or dissolved-gas reservoirs. Trans SPE AIME 1961;222:92–104.
[28] Douglas Jr J, Peaceman DW, Rachford Jr HH. A method for calculating multi-dimensional immiscible displacement. Trans SPE AIME 1961;216:297–306.
[29] Chen Z. Computational methods for multi-phase flows in porous media. SIAM 2006.
[30] Chen Z, Huan G, Li B. An improved IMPES method for two-phase flow in porous media. Transport Porous Med 2004;54:361–76.
[31] Ainsworth M, Oden JT. A posteriori error estimation in finite element analysis. John Wiley and Sons; 2000.
[32] Verfürth R. A review of a posteriori error estimation and adaptive mesh refinement techniques. New York, Stuttgart: Wiley/Teubner; 1996.
[33] Carey GF. Computational grids: generation, adaptation and solution strategiess. Taylor & Francis; 1997.
[34] Kröner D. Numerical schemes for conservation laws. Wiley/Teubner; 1997.
[35] Noelle S, Rosenbaum W, Rumpf M. 3D adaptive central schemes: part I. Algorithms for assembling the dual mesh. Appl Numer Math 2006;56(6):778–99.
[36] Karni S, Kurganov A, Petrova G. A smoothness indicator for adaptive algorithms for hyperbolic systems. J Computat Phys 2002;178(2):323–41.
[37] Tang H, Tang T. Adaptive mesh methods for one-and two-dimensional hyperbolic conservation laws. SIAM J Numer Anal 2003;41(2):487.
[38] Chen Z. Finite element methods and their applications. Springer; 2005.
[39] Guermond JL, Pasquetti R. Entropy-based nonlinear viscosity for fourier approximations of conservation laws. CR Math 2008;346(13–14):801–6.
[40] Li Y, Bangerth W. The deal.II tutorial: step-21. <http://dealii.org/developer/doxygen/deal.II/step_21.html>.
[41] Brezzi F, Fortin M. Mixed and hybrid finite element methods. Springer-Verlag; 1991.
[42] Bangerth W, Hartmann R, Kanschat G. deal.II – a general purpose object oriented finite element library. ACM Trans Math Softw 2007;33(4):24/1–24/27.
[43] Kronbichler M, Bangerth W. The deal.II tutorial: step-31. <http://dealii.org/developer/doxygen/deal.II/step_31.html>.
[44] Neckels D, Bangerth W. The deal.II tutorial, step-33. <http://dealii.org/developer/doxygen/deal.II/step_33.html>.
[45] Zhang F. The Schur complement and its applications. Springer; 2005.
[46] Bangerth W. The deal.II tutorial: step-20. <http://dealii.org/developer/doxygen/deal.II/step_20.html>.
[47] Nitta I, Hottinen T, Himanen O, Mikkola M. Inhomogeneous compression of PEMFC gas diffusion layer: part I. Experimental. J Power Source 2007;171(1):26–36.
[48] Hottinen T, Himanen O, Karvonen S, Nitta I. Inhomogeneous compression of PEMFC gas diffusion layer: part II. Modeling the effect. J Power Source 2007;171(1):113–21.
[49] Bazylak A, Sinton D, Liu ZS, Djilali N. Effect of compression on liquid water transport and microstructure of PEMFC gas diffusion layers. J Power Source 2007;163(2):784–92.
[50] Lister S, Sinton D, Djilali N. Ex situ visualization of liquid water transport in PEM fuel cell gas diffusion layers. J Power Source 2006;154(1):95–105.